Preliminary three-dimensional analysis of the heliospheric response to the 28 October 2003 CME using SMEI white-light observations

B. V. Jackson,[1] A. Buffington,[1] P. P. Hick,[1] X. Wang,[1] and D. Webb[2]

[1]   The Solar Mass Ejection Imager (SMEI) has recorded the inner heliospheric response in white-light Thomson scattering to the 28 October 2003 coronal mass ejection (CME). This preliminary report shows the evolution of this particular event in SMEI observations, as we track it from a first measurement at approximately $20°$ elongation (angular distance) from the solar disk until it fades in the antisolar hemisphere in the SMEI $180°$ field of view. The large angle and spectrometric coronagraph (LASCO) images show a CME and an underlying bright ejection of coronal material that is associated with an erupting prominence. Both of these are seen by SMEI in the interplanetary medium. We employ a three-dimensional (3-D) reconstruction technique that derives its perspective views from outward flowing solar wind to reveal the shape and extent of the CME. This is accomplished by iteratively fitting the parameters of a kinematic solar wind density model to both SMEI white-light observations and Solar-Terrestrial Environment Laboratory (STELab), interplanetary scintillation (IPS) velocity data. This modeling technique separates the true heliospheric signal in SMEI observations from background noise and reconstructs the 3-D heliospheric structure as a function of time. These reconstructions allow separation of the 28 October CME from other nearby heliospheric structure and a determination of its mass. The present results are the first utilizing this type of 3-D reconstruction with the SMEI data. We determine an excess-over-ambient mass for the southward moving ejecta associated with the prominence material of 7.1×10^{16} g and a total mass of 8.9×10^{16} g. Preliminary SMEI white-light calibration indicates that the total mass of this CME including possible associated nearby structures may have been as much as $\sim 2.0 \times 10^{17}$ g spread over much of the earthward facing hemisphere.

1.   Introduction

[2]   The 28 October 2003 coronal mass ejection (CME) was, by all standards, an exceptional solar event. The initial CME shock response took 20.3 hours to reach Earth [*Cliver and Svalgaard*, 2004], one of the fastest recorded transit times to date. (The fastest CME shock response to date on record on 4–5 August 1972 traveled from Sun to Earth in a brief 14.6 hours [*Cliver et al.*, 1990].) The Solar Mass Ejection Imager (SMEI) [*Eyles et al.*, 2003; *Jackson et al.*, 2004] measures Thomson-scattered sunlight with a broadband spectral response viewing most sky globally around the Earth. SMEI successfully recorded all-sky images at this time, except for an ~ 1 day outage beginning at ~ 0000 UT,

30 October 2003 just after the bulk of the CME event arrived at Earth.

[3]   SMEI was launched 6 January 2003 on the Air Force Space Test Program satellite Coriolis (Figure 1). Using a combination of three-dimensional (3-D) modeling and image analysis techniques, the SMEI observations can quantify the 3-D extents of transient and corotating heliospheric structures and their interactions with each other and slow-moving ambient solar wind. Precisely calibrated SMEI images are required for displaying typical slow and fast-moving heliospheric structures in 2-D sky maps and for their 3-D reconstructions.

[4]   In this article we use the term "CME" to include various aspects of a sequence beginning with the ejection of material from the corona that then moves outward into the heliosphere. In this paper we show first-time SMEI results. From the heliospheric SMEI data alone it is impossible to separate the original coronal material forming the mass ejection as it is observed by coronagraphs, from the ambient coronal and heliospheric material affected ("swept up") by the passage of the CME. Thus the term CME in the context of this paper is used to describe a process that includes both the

[1]Center for Astrophysics and Space Sciences, University of California, San Diego, La Jolla, California, USA.
[2]Institute for Space Research, Boston College, Chestnut Hill, Massachusetts, USA.

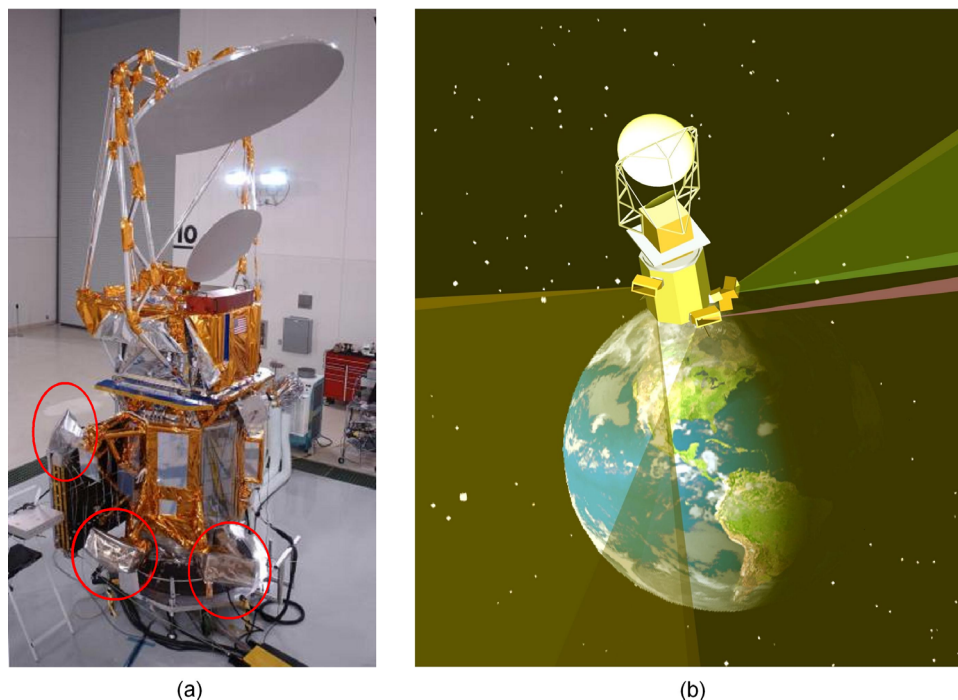(a)   (b)

Figure 1. (a) The Coriolis spacecraft with the Solar Mass Ejection Imager (SMEI) on board prior to launch from Vandenberg AFB. The three SMEI camera baffles (circled) are seen on the lower portion of the spacecraft. The Windsat antenna is at the top. (b) SMEI in its terminator polar orbit at 840 km with an orbital inclination of 98°. SMEI looks away from the Earth at 30° above the local horizontal to avoid sunlight reflected from the Earth and from the Windsat antenna. The fields of view of the three cameras (each shown as shaded wedges extending from the satellite) together cover nearly 180° of sky and, as the instrument orbits Earth, sweep out nearly the whole sky around it.

"original" CME ejecta and the induced responses in the outer corona and heliosphere (where it is observed by SMEI).

[5] Section 2 briefly describes the University of California, San Diego (UCSD) 3-D analysis techniques used here to analyze SMEI data. These techniques and results presented here using SMEI data for the first time include the 3-D solar wind reconstructions that in turn provide enhanced SMEI sky maps of the 28 October CME as well as a series of 3-D views displaying outward motion for different portions of the CME. Section 3 presents the results of these analyses, locations, volumes, and masses of the CME. We conclude in section 4.

2. SMEI Analysis Techniques

2.1. UCSD SMEI Data Frame Processing

[6] Telemetry data from SMEI are relayed from the ground stations to the Air Force Research Laboratory (AFRL) data processing center at Sacramento Peak Observatory, Sunspot, New Mexico. There data packets are concatenated and the individual CCD camera data frames are decompressed and combined with spacecraft pointing information derived from a star tracker. The resulting data frames arrive at UCSD via an internet file transfer process (FTP). Hanscom also derives "pipeline processing" all-sky images for each orbit, with a coarser angular and photometric resolution. These are useful for detecting many CMEs and are available to the public in near real time at http://smei.nso.edu/index.html. At UCSD we maintain a

database of these SMEI data frames in near real time on a local server. Our colleagues at Sacramento Peak also maintain an archive of original SMEI data and display orbit-by-orbit SMEI sky map differences in near real time for public viewing.

[7] The UCSD analysis sequence processes individual SMEI data frames to produce a heliospheric sky map for every orbit of data. These maps retain the original 0.2° SMEI angular resolution and are optimized for photometric accuracy. Briefly, we (1) identify and remove corrupted and saturated data frames; (2) remove the electronic offset, subtract a dark-current contribution, and perform geometrical optical and flat field corrections for each frame; (3) register the photometric measurements onto a standard sidereal coordinate frame; (4) remove cosmic-ray particle and space-debris contributions and combine ∼1500 frames from each camera to form an all-sky map for each orbit; and finally (5) convert the resulting sidereal map as desired to different coordinate projections: sidereal or Sun-centered, fisheye, or all-sky Hammer-Aitoff. Additional detail about this part of the analysis is found in the work of *Jackson et al.* [2004].

[8] Since light from the sidereal sky (stars, the Milky Way, bright nebulae, and galaxies) is much brighter than the variable heliospheric Thomson-scattered signal, contributions from these must be subtracted from the orbital sky maps. The simplest way to remove this background is by subtracting Sun-centered sky maps from orbits adjacent in
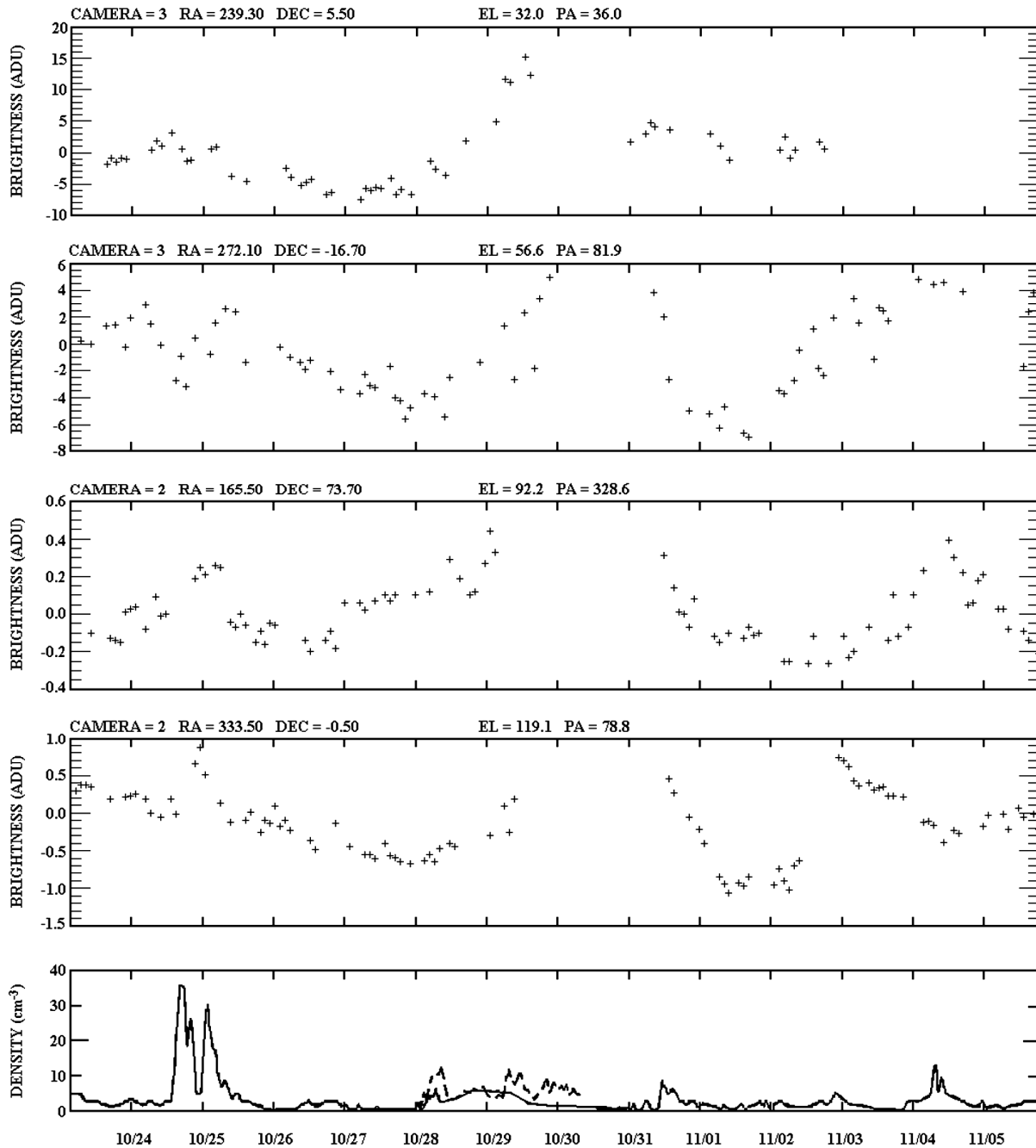
Figure 2. (top four panels) A sample of time series for 195 SMEI orbits from 23 October to 5 November 2003 from one square degree sky bins at the right ascension (RA), declination (DEC) and also at the 1200 UT, 29 October elongation (EL) and position angle (PA) locations indicated. A large brightness enhancement is first seen at the end of the day on 28 October in these sequences, especially nearest the Sun. The disturbance shows as a broad peak persisting more than a day. (bottom panel) ACE in situ solar wind density time series (hourly averages) and velocity (not shown) shows that the enhancement reaches Earth early 29 October and continues well into the following day. Wind, CELIAS, Geotail, and ACE in situ measurements for this event all provide significantly different density values, and the original ACE density rise on 28–29 October to 80 cm^{-3} has been revised as shown above [*Skoug et al.*, 2004] and is no longer thought to be as large as in early measurements. Geotail Plasma Wave Instrument values for this period are given as a dashed line (T. Terasawa, private communication, 2005).

time ("running differences"); a constant heliospheric signal present in both orbits cancels in the difference map, so in effect only the change in the heliospheric signal over the orbital time period, $\Delta t = 102$ min, is measured. *Tappin et al.* [2004] used this method to display observations of the heliospheric response to a halo CME that originated on the Sun on 28 May 2003 and was observed by SMEI on 29 May. More than 140 such events have been observed in the SMEI data to date by this method; of these, about half were likely associated with CMEs observed in the solar and heliospheric observatory (SOHO) large angle and spectrometric coronagraph (LASCO) data (XD. Webb et al., manuscript in preparation, 2006).

[9] Alternatively, a sidereal sky map averaged over orbits covering many days close to the heliospheric event can be subtracted from the orbits containing the event itself. This method preserves more of the heliospheric signal by effectively enlarging the timescale Δt to many days and is the method used in the present analysis. In addition, we have removed a zodiacal cloud brightness by fitting an analytic model to these data in a Sun-centered reference frame. The removal of this signal minimizes large changes with time of the sidereal background light from this source, especially near the Sun. The basic data used here for 3-D reconstruction consist of photometric time series at selected sidereal line-of-sight sky locations. To avoid possible contributions from bright or variable stars, analysis is further restricted to those lines of sight farther removed than $1.5°$ from any star brighter than sixth magnitude. To remove unwanted trends over time due to incompletely removed zodiacal light, background light, or long-term instrument variation, each line of sight has a running mean baseline of about 1 week duration removed from it. We conclude that this current UCSD analysis provides a stable baseline over timescales of several weeks without sacrificing angular resolution: this is sufficient for analyzing transient heliospheric disturbances and the 3-D reconstructions presented here.

[10] Figure 2 presents a sample time series from the ~1100 sky locations used for the present analysis of the October 2003 data. These were selected from an original group of ~4000 evenly spaced sidereal locations, each averaged to include one square degree of sky. Brightness for these data is given in camera analog-to-digital units (ADU). A natural unit for surface brightness in the present work is "S10," the equivalent of the brightness of a tenth magnitude solar-type star spread over one square degree of sky. Preliminary calibration of the data (to an accuracy of about 10%) using "G-star" brightnesses observed in a prototype SMEI camera operated on the ground gives 1 S10 = 0.55 ADU. We are currently deriving the equivalent numbers for each flight camera. These time series are edited to remove auroral light. Bright auroral light at heights above 840 km was discovered unexpectedly by SMEI [*Jackson et al.*, 2004; *Mizuno et al.*, 2005]. This contribution is removed by editing the time series. Auroral light is present at times of geoactivity and when SMEI passes through the auroral ovals. For the 28 October 2003 event the aurora onset time occurs when the CME impacts Earth. To remove the aurora, SMEI time series sequences are displayed in time and by orbit. Those data points that are contaminated by auroral light as recognized by orbit location and time are deleted from the time series by an automatic procedure that first cuts abrupt brightness value changes above limits unlikely for CME signals, and then deletes any remnant of the signal to the edge of this deletion in location and time. The ~1100 time series in turn produce approximately 80,000 valid lines of sight over a 2-week interval centered on the CME arrival at Earth. The 80,000 number is sufficiently redundant to support a 3-D reconstruction having a $6.7° \times 6.7°$ latitude and longitude digital resolution and half-day temporal cadence. The analysis converges to a solution within a few hours (see next section).

2.2. Three-Dimensional Reconstruction Analysis

[11] Solar physics has seen numerous attempts to reconstruct the structure of the corona and the heliosphere in three dimensions. In particular, these techniques have been developed for coronal mass ejections in order to understand the physical principles of their initiation. Employing techniques different from those used here, *Munro* [1977], *Crifo et al.* [1983], and *MacQueen* [1993] analyzed views from the Earth perspective using Thomson-scattering data. *Jackson et al.* [1985], using Helios photometer and Solwind coronagraph views from different perspectives, determined the approximate dimensions and surface origins of CMEs. *Jackson and Hick* [1994] and *Jackson and Froehling* [1995], using Helios photometer and Solwind coronagraph views from different perspectives and tomographic techniques, analyzed CMEs, and mapped their 3-D shapes.

[12] Rotational tomography of stationary solar structures (streamers) using coronagraph observations were attempted by *Wilson* [1977] and *Jackson* [1977], and more recently by *Zidowitz et al.* [1995] and *Frazin and Janzen* [2002]. Using both Helios 1 and Helios 2 photometer measurements, *Hick and Jackson* [1998] and *Jackson and Hick* [2000, 2002] fit photometric observations to a kinematic heliospheric model that incorporates both solar rotation and outward solar wind flow. The rotational tomographic analyses show that a significant enhancement in contrast between dense and less dense regions is achieved, especially during solar minimum.

[13] Interplanetary scintillation (IPS) measurements have been used to probe solar wind features since the 1960s using ground-based meter-wavelength radio observations [*Hewish et al.*, 1964; *Houminer*, 1971]. Observations from the UCSD [*Coles and Kaufman*, 1978] and Nagoya [*Kojima and Kakinuma*, 1987] multisite scintillation arrays have determined velocities in the interplanetary medium since the early 1970s. The IPS observations, resulting from a radio propagation effect caused by small-scale (~200 km) density variations, track heliospheric disturbances of larger scale that vary from one day to the next and are often associated with geomagnetic storms on Earth [*Gapper et al.*, 1982]. These observations show a predominance of disturbances that corotate with the Sun as inferred from a list of events and their associations [*Hewish and Bravo*, 1986]. Three-dimensional results from IPS observations recorded over a wide range of elongations were obtained by least squares fitting to a heliospheric model incorporating both outward solar wind flow and solar rotation [*Jackson et al.*, 1997; *Kojima et al.*, 1997; *Jackson et al.*, 1998; *Kojima et al.*, 1998; *Asai et al.*, 1998]. In the 3-D models derived from IPS analysis, scintillation strength serves as a proxy for density. In the models in these earlier papers, scintillation

strength is related to a value of small-scale density variation that is in turn scaled to bulk density and solar distance using a set of power law relationships.

[14] Early Helios photometer and IPS tomographic reconstructions assumed that the kinematic heliospheric model remains unchanged over a month-long time spanned by the observations. This implies that within this time period, the heliospheric structures remain unchanged except for outward radial expansion and solar rotation as described by the kinematic modeling. Current UCSD tomographic modeling [*Jackson et al.*, 2001, 2002; *Jackson and Hick*, 2004] relaxes this assumption, and a kinematic solar wind model formed at regular time intervals is iterated to provide the 3-D heliospheric parameters used to fit observed data. This article reports on application of this modeling technique to SMEI data for the first time. Both SMEI brightness and STELab IPS velocity are used in the solar wind reconstruction as detailed in previous papers. The large volume of data from SMEI provides finer resolution of density structures while the IPS measurements ensure that the structure overall geometry is correctly located.

2.3. Computational Analysis

[15] The computational aspects of the 3-D reconstruction program (see *Jackson et al.* [1998] and *Hick and Jackson* [2003, and references therein] for a more mathematical derivation of this process) necessarily include the detailed geometry for each line of sight: the location of each within the 3-D solar wind model and its projection to a source surface reference level closer to the Sun than all lines of sight. In the present tomographic analysis scheme, Carrington maps at evenly spaced time intervals at this source surface provide model boundary conditions for 3-D solar wind velocity and density [*Jackson et al.*, 2002] that propagates outward from this surface. The 3-D solar wind model is integrated at the location and time of each line of sight and compared with observations using a least-squares technique. The line-of-sight segment projections in space and time to each source surface are known from the modeling, and they are iteratively inverted in 2-D space and time on this source surface to update boundary conditions for the model to better fit observations.

[16] In the least-squares process described above, ratios of model to observed values are monitored at each iteration to indicate a rate of convergence. Here, velocity and density corrections to the model are made separately. First, changes are made to previous velocity boundary conditions on the reference surface. Second, the 3-D model is updated and new projected locations of each line-of-sight point on the reference surface are determined. This assures that the newest values of velocity determine the 3-D model and their projections back to the source surface for each line of sight segment. Third, changes are made to previous density boundary conditions on the reference surface. Finally, the 3-D model is again updated with all the newest boundary values.

[17] The source surface Carrington maps of velocity and density are smoothed on each iteration using a 2-D Gaussian spatial filter that incorporates equal solar surface areas and a Gaussian temporal filter. These filters are predicated by the numbers of lines of sight and noise in the data and can

be varied to ensure convergence. For these preliminary 28 October 2003 analyses, the reconstruction e^{-1} filter values have been set to spatial widths of $15°$ for the IPS velocity data and $5°$ for SMEI data and temporal widths of 0.75 and 0.325 days, respectively, for IPS velocity and SMEI data. The digital coordinate resolutions for both data sets are set spatially to $6.7° \times 6.7°$ heliographic latitude and longitude and to a half day temporal cadence to approximately match the Gaussian filter resolution [see *Jackson and Hick*, 2004]. We require the amplitude of the sum of all Gaussian contributions at a single coordinate position be more than one in order that several different perspective lines of sight produce changes in the modeled values. Where the sum of all contributors is less than one, in order to obtain continuity along lines of sight, the source surface value is interpolated from locations where the data can be changed. Where the values in the model cannot be changed at some location, these coordinate positions are left blank in the final result. For the 28 October CME event SMEI data, this includes a section of heliospheric volume within the hemisphere opposite Earth that cannot be observed and reconstructed by SMEI at the $6.7°$ spatial resolution scale.

[18] This program generally converges to an unchanging model within a few iterations. The program is set to operate for nine iterations to be certain the program has converged [see *Jackson et al.*, 1998]. For a typical rotation and the digital resolutions above, a set of density and velocity iterations generally takes about 15 min on a 3.0 GHz Pentium IV computer. Those IPS velocity observations and SMEI brightness lines of sight throughout the period that do not fit within a three-sigma limit of the mean ratio change ascribed at that location by the model are removed from the data set. The program then operates for another nine iterations. We find that the model solutions are insensitive to the starting model values, and after a few iterations any signature of the initial model is lost. Other tests [see *Jackson et al.*, 1998] show that tomographically analyzing a set of artificial observations using a known 3-D input reproduces the input.

3. Analysis Results

3.1. Sky Maps

[19] Figure 3a shows a SMEI Hammer-Aitoff sky map obtained during a single orbit just as the 28 October 2003 CME arrives at Earth midday on 29 October. Figure 3a combines one orbit's worth of approximately 4500 individual $3° \times 60°$ data frames from all three SMEI cameras. The brightness scale to the left of the map is in S10 using the value 1 S10 = 0.55 ADU (section 2.1). A portion of the sky map is blanked out and not shown in the figure where too many high-energy particle hits (cosmic rays) and auroral light produce an apparent response far above the normal background. Figure 3b is a sky map resulting from the above-described 3-D reconstruction using the full set of time series (Figure 2 examples). The brightness scale is in S10. The resulting S10 scale of Figure 3b is about a factor of 10 smaller than the ADU scale of Figure 3a. The time on Figure 3a is the orbit beginning time that starts near the south ecliptic pole and increases clockwise around the map center. The time given in Figure 3b, and on
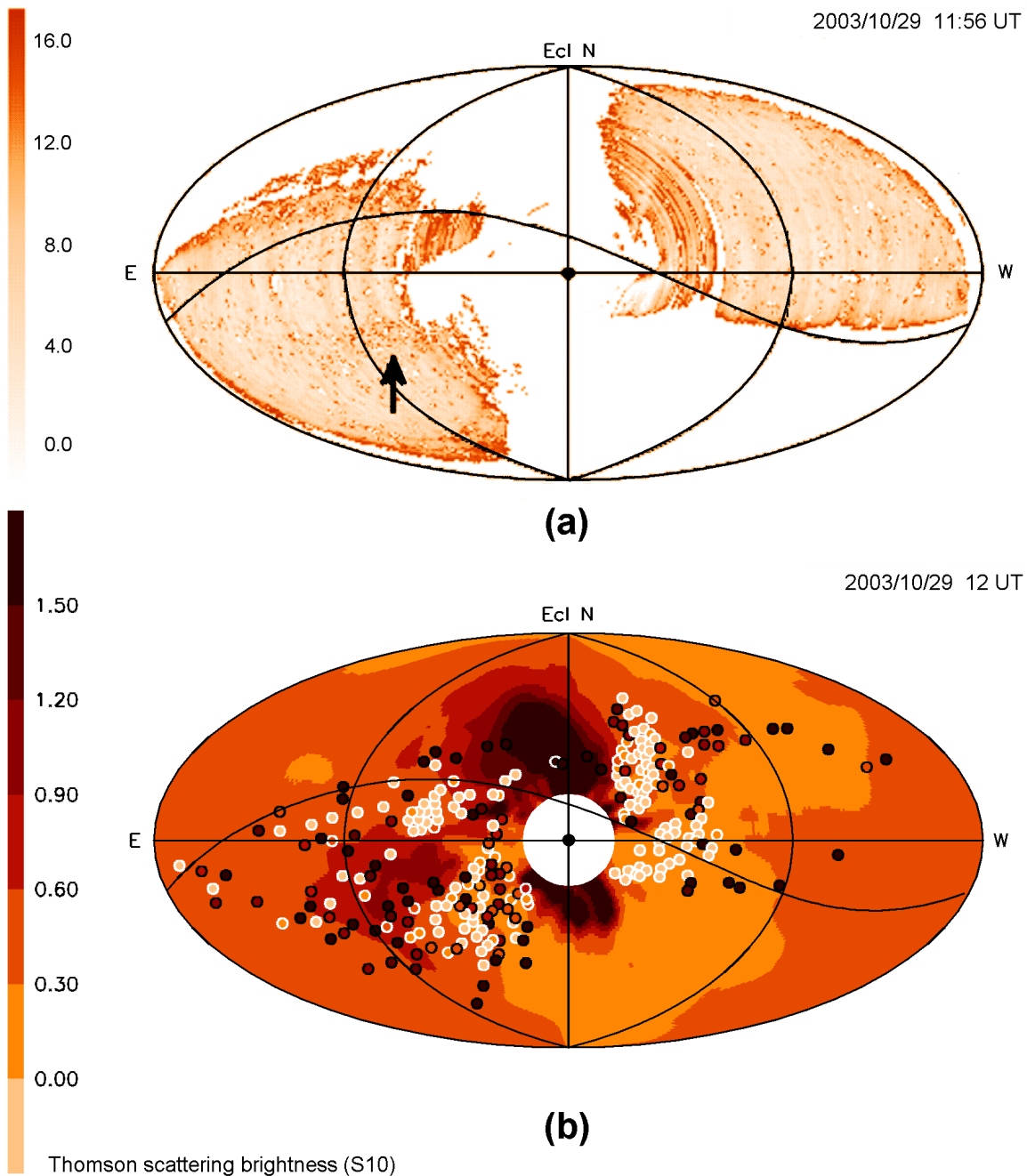
Figure 3. Sun-centered Hammer-Aitoff sky maps of the 28 October 2003 CME as viewed from SMEI (Earth). The faster portion of the CME directed toward Earth lies primarily to the solar northeast and begins to engulf Earth (reaching 90° elongation) over the whole of the map at this time. The large prominence-associated ejecta to the south of the Sun have reached about 45° elongation. The brightness scale of each map is placed to the left. (a) A direct single-orbit sky map compiled from ~4500 SMEI data frames. Brightness is in S10. Large portions of this particular map are blanked out by high-energy particle hits and auroral light. An arrow indicates a CME structure in the direct map image. (b) Sky map as derived by the edited time series and 3-D reconstructions fit to the direct images of the event as it moves outward from the Sun. The locations of all valid time series positions within a 102-min period of 1200 UT, 29 October are positioned on the map. All positions are given as a circle filled with the appropriate value along the line of sight relative to the ambient at that location. This map has an r^{-2} heliospheric density as a radial filter multiplier (see text) and is thus different from Figure 3a that does not have this radial filter applied. Also since the 3-D reconstruction in effect draws its result from the entire series of 195 sky maps for this time period, the gaps in individual maps (see text) are effectively filled by the reconstruction process.
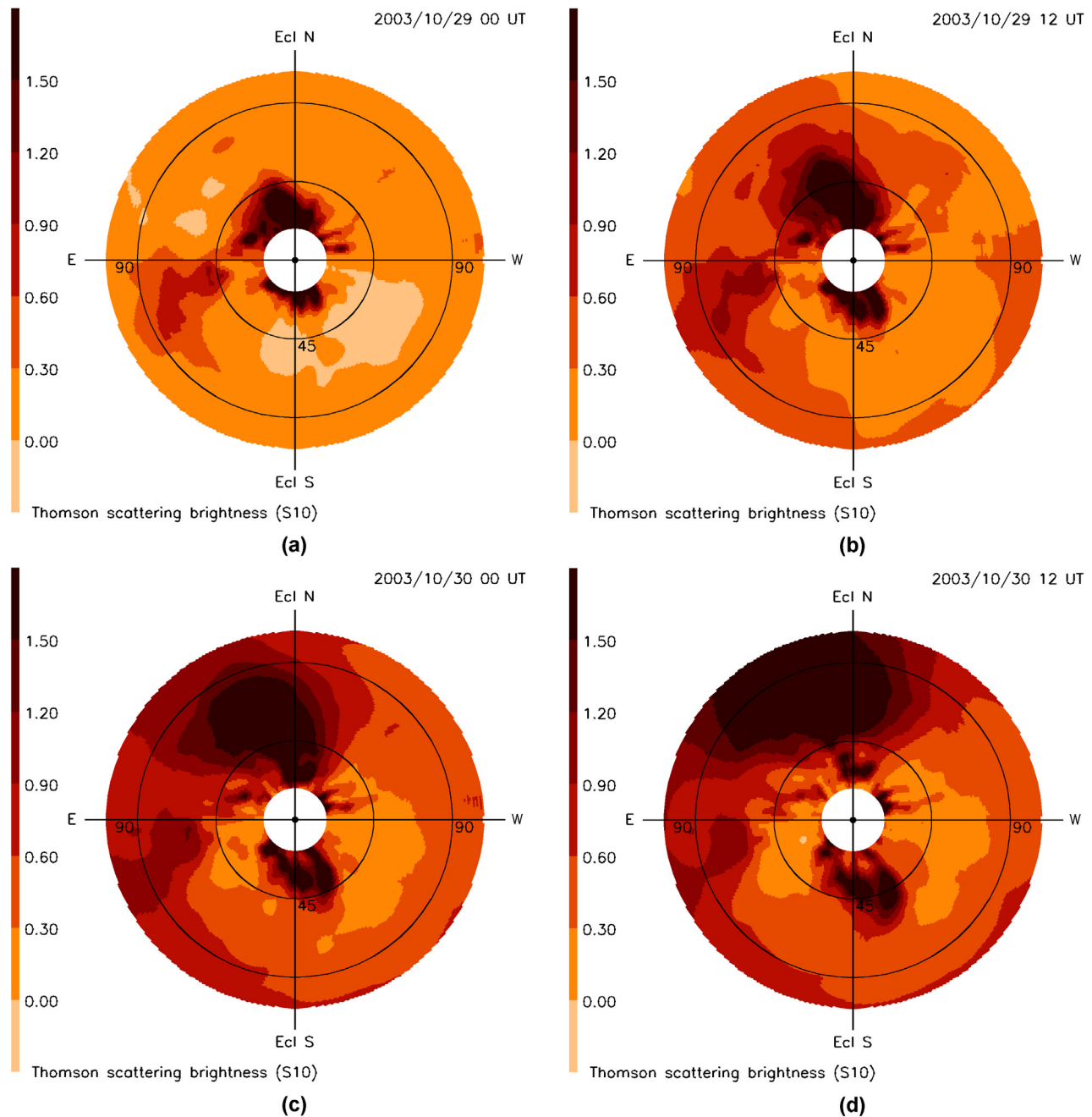
Figure 4. Sun-centered ecliptic "fisheye" sky maps as derived from the edited time series and 3-D reconstructions. These are shown out to 110° elongation as viewed from SMEI for the 28 October 2003 CME as it moves outward from the Sun over a period of two days. These maps have an r^{-2} heliospheric density normalized to unity at 90° elongation as a radial filter multiplier so that CME features can be more directly compared as they move outward. (a)–(d) The faster portion of the CME directed towards Earth lies primarily to the solar northeast and begins to engulf Earth (reach 90°) about midday on 29 October. At the same time the large prominence-associated ejecta to the south of the Sun has reached just beyond 45° elongation. Different CME portions can be observed to move outward over the next two sky maps. Since there are no data from SMEI midday 30 October 2003, the presentation at the time shown in Figure 4d is a model interpolation resulting from the time series data on either side of the gap in SMEI observations.
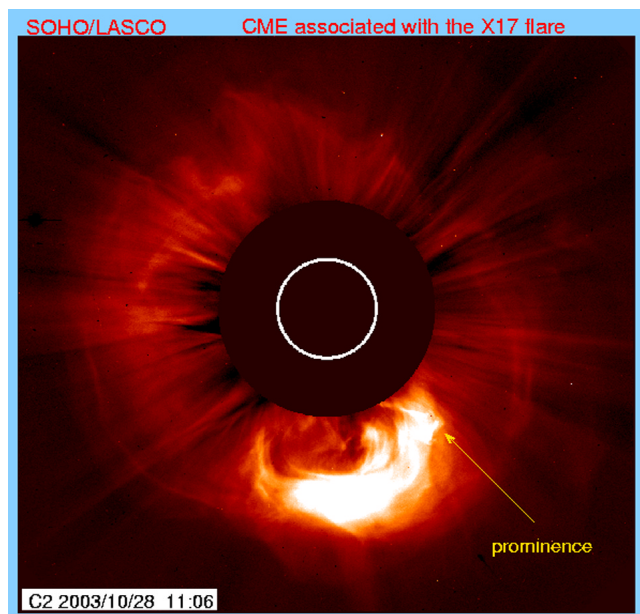
Figure 5. LASCO C2 observations of the 28 October 2003 CME. Most of the early CME response "halos" the Sun and is associated with an X17.2 flare at S16 E09 that commences at 1036 UT, 28 October. The large eruption to the south associated with a solar prominence (indicated) is also viewed to move outward over time to the south in LASCO images.

subsequent SMEI images and in tables, are instantaneous times interpolated to the appropriate value from the reconstruction analyses. In spite of data outages in individual maps from particle hits, aurora, and an outage for most of 30 October, more than enough information remains in the time series sequences to reconstruct several portions of the 28 October CME and render visible low-contrast heliospheric features difficult to see in individual sky maps. These include part of the CME to the northeast of the Sun, not much evidence of a solar halo of bright material elsewhere, and another bright structure ejected to the south. Additional bright material in these sky maps to the southeast in Figure 3b is probably associated with an earlier series of bright CMEs observed by LASCO midday 26 October and early 27 October. The 3-D reconstructed volumes have an r^{-2} density gradient removed from them relative to the nominal 1 AU density so that heliospheric features at large solar elongation have approximately the same brightness as those close to the Sun when projected as a sky map as in Figure 3b. Thus these reconstructed sky maps are somewhat unlike the direct single-orbit sky map of Figure 3a where this radial gradient has not been removed.

[20] Few other remote-sensing heliospheric observations of this series of events exist. The STELab, Japan IPS observations [*Tokumaru et al.*, 2005] map little data to the south at this time of year and thus missed most of the eruption of the large southward directed prominence-associated ejecta. The IPS scintillation level response does, however, show an enhancement primarily to the solar northeast and little to the west, consistent with SMEI data.

3.2. Three-Dimensional Reconstruction Presentation

[21] Figures 4a–4d present a sequence of "fisheye" sky maps similar to Figure 3b and show the progression of the CME outward in 2-D sky maps. The sky maps are derived from the density volumes that have been fit to the observed data by integrating through the volumes and summing the total line of sight brightness [*Billings*, 1966]. The volumes have an r^{-2} heliospheric density normalized to unity at 90° elongation as a radial filter multiplier. Thus the sky maps from them better show the outward progression of heliospheric structures both before and interpolated to the middle of the 1-day data outage that began at ∼0000 UT, 30 October. In addition, these sky maps from the tomographic modeling have a 5 e^- cm^{-3} base removed from them and thus present excursions from a mean of zero much as the time series of Figure 2. Because the fit to a heliospheric solar wind model uses time series from multiple sky maps and helps remove signals that do not participate in the outward progression of the solar wind, bad spots in the data can be filled in to provide continuous coverage. In addition, since few unwanted signals remain, the scale of the map excursions can be enhanced above those of direct sky maps, and thus far more detail can be discerned in them. This analysis shows not only the bright heliospheric CME response primarily to the solar northeast that engulfs the Earth but also details of the large prominence and white-light eruption first observed in the LASCO coronagraph (Figure 5). This moves outward into the heliosphere and passes south-southeast of the Earth. An earlier slower-moving disturbance to the solar southeast that began its outward motion on about 0000 UT, 27 October 2003 is also seen in this sky map sequence.

[22] The 3-D density distribution from which these sky maps were derived allows results to be viewed from any vantage point, not just from Earth. Since several heliospheric structures often overlap along a line of sight, determination of their 3-D extent has the advantage of more completely allowing measurement of the direction of travel and the masses of structures over time. Figures 6a–6d show a 3-D reconstruction of this CME at four times as a remote observer would view the event from 30° above the ecliptic plane and about 45° west of the Sun-Earth line. Only the portion of the heliospheric volume on the earthward side of the Sun within 110° of Earth's longitude is depicted in this reconstruction. The 3-D resolution is presently limited by the numbers of lines of sight used in the analysis, here far fewer than will ultimately be available. There are several reasons that all brightness lines of sight cannot be used this time, and chief among these is computational; current 3-D reconstruction algorithms can only easily handle a total of ∼200,000 lines of sight. Although more lines of sight will ultimately be used, we do not expect these to significantly affect the shape of the event, only its detail. Even so, these reconstructions show that the fast portion of the CME engulfing Earth was far more extensive and dense to the solar northeast than in other directions. The analysis also shows that a portion of the connected density structure extends back to near the prominence ejection and that the prominence begins to break up into separate pieces in the inner heliosphere. Better views of the direction of travel of these features are shown in another set of fisheye sky
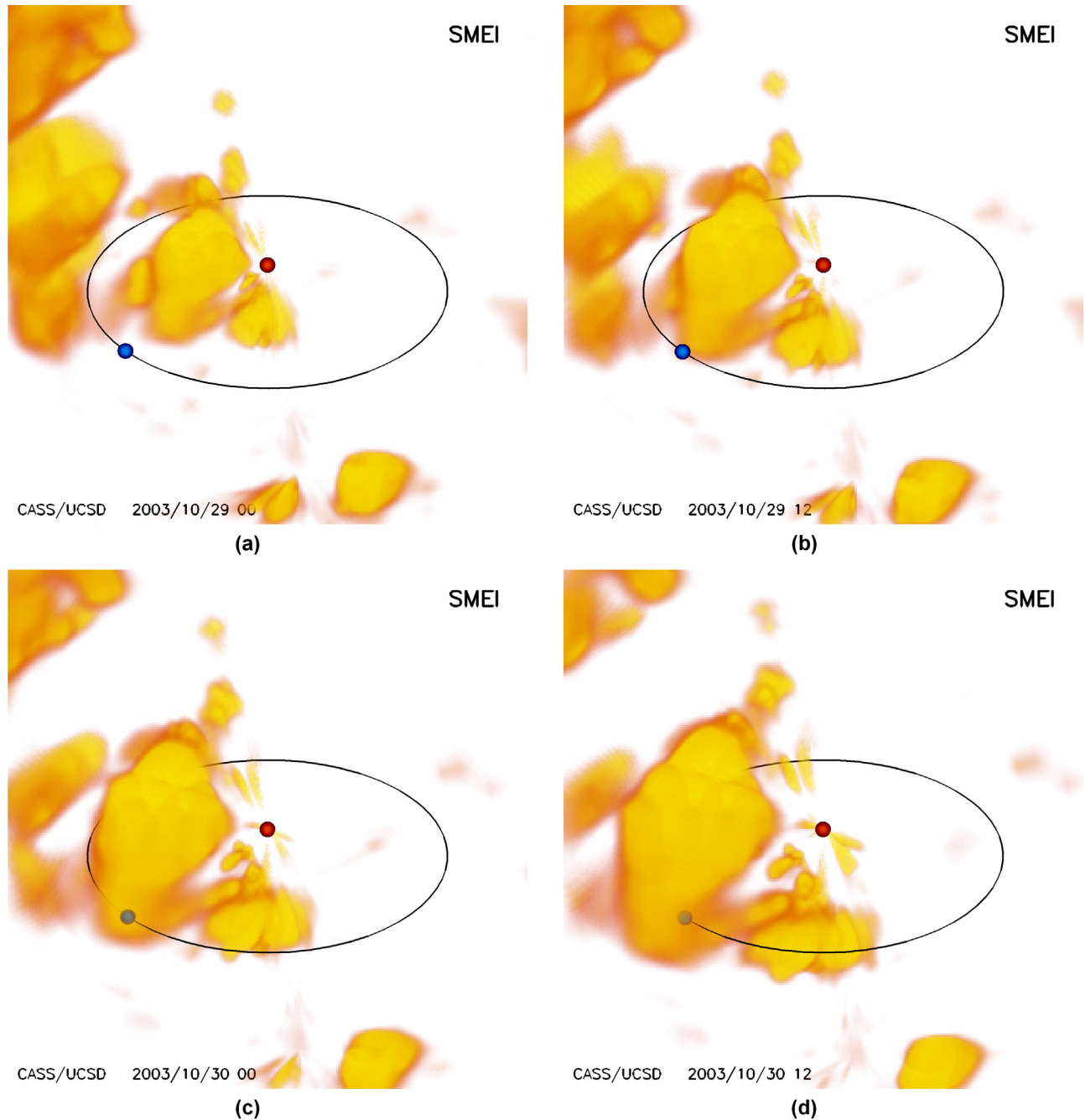
Figure 6. Three-dimensional reconstructions at four successive times of the heliospheric response to the 28 October 2003 CME as viewed from 3AU 30° above the ecliptic plane and ~45° west of the Sun-Earth line. The location of the Earth is indicated by a blue circle with the Earth's orbit viewed in perspective drawn as an ellipse. The Sun is indicated by a red dot. Densities are contoured between 10 and $30e^- cm^{-3}$ and have an r^{-2} density gradient removed from them. The fast structure moving to the solar northeast as observed from Earth is the dominant object here. The ejecta associated with the solar prominence are observed to the south of the Sun in these views. The heliospheric response to CMEs moving to the solar southeast are partially observed behind the faster moving object that engulfs Earth in Figures 6c and 6d.

maps that are centered on the anti-solar direction (Figures 7a–7d). Here, the fast portion of the CME vanishes to the solar northeast while ejecta associated with the prominence move off to the solar southwest. The

line-of-sight observations producing these sky maps are more numerous toward Sun but also provide a good sampling within the area covered by the original maps. Thus Figure 7 maps may not correspond as closely to the
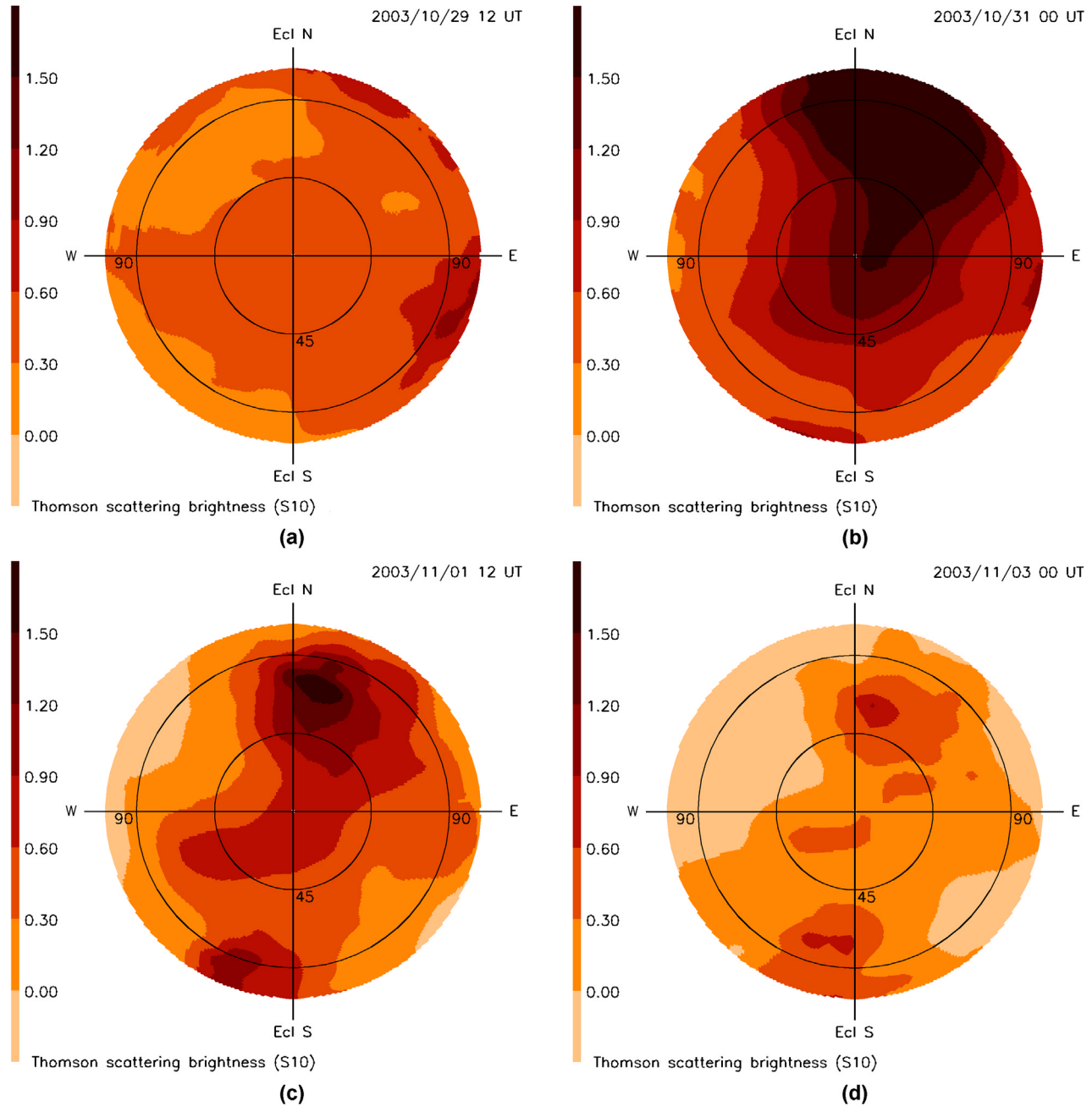
Figure 7. Fisheye sky maps of the 28 October 2003 CME directed $180°$ from the Sun. (a)–(d) Sky maps as derived by the edited time series and 3-D reconstructions shown at intervals of one and a half day. Figure 7a has the same time in common with Figure 3, Figure 4b, and Figure 6b and includes some of the same structure since these maps extend to $110°$ from the center. The bulk of the portion of the CME that engulfed Earth fades away at about $45°$ from the Sun-Earth line.

direct sky maps in this direction of space, as would an average including all the line-of-sight observations.

3.3. CME Mass

[23] In these analyses we assume one electron is associated with 2.0×10^{-24} g of mass, a combination of 10% helium ions and 90% hydrogen ions [*Hildner et al.*, 1975], and that all solar material is completely ionized at the distances from the Sun that SMEI measures brightness.

The CME mass derived for this event is made up of two portions that include an ambient that is swept up and moved outward by the large pulse of energy input to the lower corona, and a portion (the original CME) that was expelled from the low corona during the event. Although we cannot distinguish unambiguously between these two mass types from the SMEI analysis alone, we can model both with solar distance. To do this, we assume a standard heliospheric background ambient mass by noting this ambient value

Table 1. Three-Dimensional CME Masses Derived for the 28 October 2003 CME

	First Recon. Time	Lower Contour, e^-cm^{-3}	Excess Mass, $\times 10^{16}$g	Total Mass, $\times 10^{16}$g	Second Recon. Time	Lower Contour, e^-cm^{-3}	Excess Mass, $\times 10^{16}$g	Total Mass, $\times 10^{16}$g
Earth-directed density	29 Oct, 1200 UT	10.0	6.7	8.3	30 Oct, 0000 UT	10.0	6.9	8.6
Total CME	29 Oct, 1200 UT	10.0	13.6	16.9	30 Oct, 0000 UT	10.0	14.0	17.2
Total CME excluding previous west event	29 Oct, 1200 UT	4.0	~12.3	~16.8	30 Oct, 0000 UT	4.0	~15.1	~20.5
Prominence-associated ejecta, a	30 Oct, 0000 UT	30.0	0.77	0.88	31 Oct, 0000 UT	30.0	0.70	0.80
Prominence-associated ejecta, b	30 Oct, 0000 UT	30.0	1.45	1.61	31 Oct, 0000 UT	30.0	1.51	1.69
Prominence-associated ejecta, total	30 Oct, 0000 UT	10.0	7.10	8.81	31 Oct, 0000 UT	10.0	7.11	8.93

from in situ data at 1 AU. Using the location and volume of the CME structure, and with knowledge of the velocity of the outward structure, we derive an ambient mass at the position of the CME defined within the contour interval. An excess and total mass for the CME follows from this ambient model. In general for large events, the ambient is only a small portion of the total structure mass. We assume that the various density structures of this CME are all part of the same event, since all erupt from the Sun at the same time. At the lowest density contours a bridge of mass extends from the fast-moving material northeast of the Sun to the more slowly moving dense structure associated with the prominence eruption to the solar southwest. For ejecta associated with the prominence, this modeling effort is not difficult since the structure is fairly isolated from the rest of the CME and has a reasonably well-defined shape. We determine values for two portions of this structure at a contour level (30 e^- cm^{-3}) where they become well separated. The core of the first (or "a") portion of this structure in Table 1 lies nearly parallel to the observer's line of sight, is somewhat more dense than the other, and its near end is closer to Earth. The second ("b") portion (see Figure 8) spreads over a large range of longitudes and its center moves outward about 70° from the Sun-Earth line. As for excess and total mass, it is not possible to tell what portion of the ejecta is associated solely with Hα prominence material, but in all likelihood the denser portion of the "a" structure retains some of the shape and material of this originally less-ionized material.

[24] Table 1 lists the masses obtained for various parts of this CME. Determinations of mass are made at two different times as the material moves outward as a check on the technique. The CME structure close to the Sun is better defined but contains less volume for accurate measurement: thus unless otherwise noted, measurements at both times should be given equal weight. The earthward directed structure moves more rapidly than the southward directed component, so measurements of the latter are necessarily obtained later in time when it has reached greater distances from the Sun. Table 1 names the structure measured in the first column. The reconstruction times for the measured structures are given in columns 2 and 6. The volume of the structure is limited by a 3-D contour so that except for the third entry (total CME excluding previous west event) the structure is isolated from others. A lower contour interval used to define the structure is usually set to a value twice the ambient or 10 e^- cm^{-3}. This somewhat arbitrary value is intended to be used so that one CME structure can

be isolated from another. A value lower than this incorporates more volume and mass and a higher value incorporates less. Mass values as high as 100 e^- cm^{-3} can often be observed at the center of large CME structures, and thus for most dense events the choice of an outer contour interval is not a critical factor in determining the total mass of the CME. These contour levels are given in column 3 and
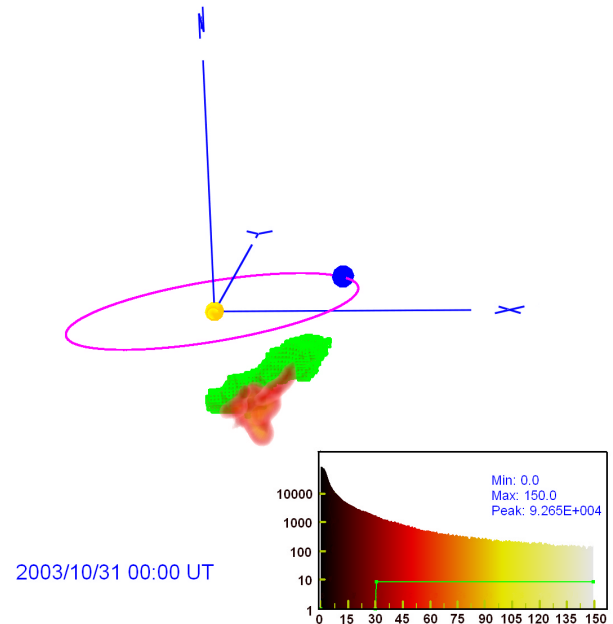

Figure 8. Mass measurement of the prominence-associated ejecta a portion of the 28 May CME (highlighted in green) as described in the text. The view is from about 20° north of the ecliptic plane, and 110° east of the Sun-Earth line. The axes are heliographic coordinates with the x-axis pointed in the direction of the heliographic longitude of the vernal equinox. The ecliptic is shown as a purple ellipse. Dense foreground portions of the CME (see Figure 6) have been removed by cutting planes leaving this portion of the event easy to view. Part of the more southward "b" portion of the prominence ejecta lies below and in front of the highlighted "a" portion from this viewpoint. The insert to the lower right of the figure gives a histogram of the number of volume elements at different densities, their colors, and the selected lower contour level at 30 e^- cm^{-3}. The total mass is highlighted in green and in the table is 8×10^{15}g and the volume is 0.014 AU^3 (see Tables 1 and 2).

Table 2. Three-Dimensional CME Volumes and Location for the 28 October 2003 CME

	First Recon. Time	Lower Contour, e^- cm^{-3}	Volume, AU^3	Centroid, AU, deg	Upper Limit, AU, deg	Lower Limit, AU, deg	Lat. Extent, AU, deg	Long. Extent, AU, deg
Earth-directed density	29 Oct, 1200 UT	10.0	0.226	0.70	1.13	0.31	130	90
				+30	0	50		
				−5	0	0		
Total CME	29 Oct, 1200 UT	10.0	0.308	0.70	1.13	0.17[a]	170	205
				+30	0	−70[a]		
				−5	0	10[a]		
Total CME excluding previous west event	29 Oct, 1200 UT	4.0	0.860	0.70	1.14	0.17[a]	180	205
				+30	0	−70[a]		
				−5	0	10[a]		
Prominence-associated ejecta, a	31 Oct, 0000 UT	30.0	0.014	0.67	0.80	0.41	40	75
				−40	−40	−55		
				25	15	55		
Prominence -associated ejecta, b	31 Oct, 0000 UT	30.0	0.015	0.56	0.81	0.35	30	200
				−75	−75	−75		
				15	20	10		
Prominence-associated ejecta, total	31 Oct, 0000 UT	10.0	0.119	0.56	0.87	0.30	70	205
				−75	−75	−75		
				15	20	20		

[a]Values extrapolated from later times.

column 7 of Table 1. Excess and total mass at the different times for these structures are given in columns 4 and 5 and 8 and 9, respectively. We show more significant figures for mass than accuracy warrants in order to display differences between excess and total mass. Accuracy varies with structure and most measurements include a host of factors inherent in the kinematic solar wind model, the ambient solar wind determination, and potential systematic errors such as residual auroral light and uncertainty in the SMEI brightness calibration. These modeling factors and systematic errors affect both the mass and the lower contour interval, and we expect the present mass estimates to be no more accurate than ∼20%.

[25] Since few other papers in the literature detail this method of determining heliospheric mass [e.g., *Wang et al.*, 2003] the technique used here is demonstrated in Figure 8 for an example structure (the fourth entry, or "a" portion of the prominence-associated ejecta on 0000 UT, 31 May). A 3-D contour level is set to isolate the mass of the structure from others, and cubes that occupy the volume within the contour then approximate the heliospheric structure. The sum of the mass within these cubes determines the total mass of the structure, and the summed volume of the cubes gives the heliospheric volume of the structure. By assuming an ambient solar wind (we here use a value of 5 e^- cm^{-3} at 1 AU with an r^{-2} falloff as used for the 3-D reconstruction), we obtain a value of excess mass above the ambient within this contour as a difference of the total mass and the ambient.

[26] Table 2 gives more information about the 28 October 2003 CME from the 3-D reconstructions. Here each structure is again listed, followed by its reconstruction time in column 2. Column 3 gives the lower contour interval used to define the structure, the same as for the values in Table 1. Structure centroid location and upper and lower limits are given by three numbers, respectively: height in AU and ecliptic latitude and longitude in degrees relative to Earth (east minus, west plus). Although measurement errors for these analyses are generally about 0.01 AU and a few degrees, these values are interpolations to far coarser location measurements, as stated previously, and assume that the density values vary smoothly throughout the volume. Occasionally, the reconstructed structure lies outside of the volume SMEI can view. In this case the "measurements" are tomographic extrapolations and presumed less accurate than values where there was a direct view, and these values are marked. The inner boundary source surface was chosen to be at 15 Rs. The Table 2 centroid locations are probably more accurately determined by these analyses than the volumes and structure extents since the latter depend not only upon the assumptions inherent in the kinematic modeling but also on the location of the lower contour interval from the SMEI brightness calibration that currently has a precision of ∼10%.

4. Conclusion

[27] White-light Thomson scattering observations from SMEI have recorded the inner heliospheric response to the 28 October 2003 CME. This paper shows the extent of the CME in SMEI observations, and we are able to track the event from its first measurement approximately 20° from the solar disk until it vanishes from the SMEI field of view on the side of Earth opposite the Sun. Several portions of the CME can be followed into the interplanetary medium associated with the initial CME response and the underlying erupting prominence structure. The present work is the first application of UCSD 3-D tomography to the photometric SMEI data, and these preliminary results are very encouraging. The technique obtains perspective views of outward flowing solar wind and allows separating the heliospheric response from other sources of background noise, filling in regions of missed or noisy data, and determining the 3-D structure of the CME and estimating its mass. The analysis shows details of the CME as it evolves outward past Earth but is preliminary because significantly improved results both in photometric precision and angular resolution will be available as we further refine the SMEI analysis

algorithms and include more lines of sight. Also, more sophisticated 3-D modeling techniques will hopefully refine observational fits to the data.

References

Asai, K., M. Kojima, M. Tokumaru, A. Yokobe, B. V. Jackson, P. L. Hick, and P. K. Manoharan (1998), Heliospheric tomography using interplanetary scintillation observations: 3. Correlation between speed and electron density fluctuations in the solar wind, *J. Geophys Res.*, *103*, 1991.

Billings, D. E. (1966), *A Guide to the Solar Corona*, p. 150, Elsevier, New York.

Cliver, E. W., and L. Svalgaard (2004), The 1859 solar-terrestrial disturbance and the current limits of extreme space weather activity, *Solar Phys.*, *224*, 407–422.

Cliver, E. W., J. Feynman, and H. B. Garrett (1990), An estimate of the maximum speed of the solar wind, 1938–1989, *J. Geophys Res.*, *95*, 17,103.

Coles, W. A., and J. J. Kaufman (1978), Solar wind velocity estimation from multistation IPS, *Radio Sci.*, *13*, 591.

Crifo, F., J. P. Picat, and M. Cailloux (1983), Coronal transients: Loop or bubble?, *Solar Phys.*, *83*, 143.

Eyles, C. J., G. M. Simnett, M. P. Cooke, B. V. Jackson, A. Buffington, P. P. Hick, N. R. Waltham, J. M. King, P. A. Anderson, and P. E. Holladay (2003), The Solar Mass Ejection Imager (SMEI), *Solar Phys.*, *217*, 319.

Frazin, R. A., and P. Janzen (2002), Tomography of the solar corona. II. Robust, regularized, positive estimation of the three-dimensional electron density distribution from LASCO-C2 polarized white-light images, *Astrophys. J.*, *570*, 408.

Gapper, G. R., A. Hewish, A. Purvis, and P. J. Duffett-Smith (1982), Observing interplanetary disturbances from the ground, *Nature*, *296*, 633.

Hewish, A., and S. Bravo (1986), The sources of large-scale heliospheric disturbances, *Solar Phys.*, *106*, 185.

Hewish, A., P. F. Scott, and D. Wills (1964), Interplanetary scintillation of small diameter radio sources, *Nature*, *203*, 1214.

Hick, P., and B. V. Jackson (1998), Three-dimensional tomography of heliospheric features using Thomson-scattering data, *Proc. SPIE*, *3442*, 87.

Hick, P. P., and B. V. Jackson (2003), Heliospheric tomography: An algorithm for the reconstruction of the 3D solar wind from remote sensing observations, *Proc. SPIE*, *5171*, 287.

Hildner, E., J. T. Gosling, R. M. MacQueen, R. H. Munro, A. I. Poland, and C. L. Ross (1975), The large coronal transient of 10 June 1973 I: Observational description, *Solar Phys.*, *42*, 163.

Houminer, Z. (1971), Corotating plasma streams revealed by interplanetary scintillation, *Nature Phys. Sci.*, *231*, 165.

Jackson, B. V. (1977), A coronal hole equatorial extension and its relation to a high speed solar wind stream, paper presented at Topical Conference on Solar and Interplanetary Physics, Univ. of Ariz., Tucson, Ariz.

Jackson, B. V., and H. R. Froehling (1995), Three-dimensional reconstruction of a coronal mass ejection, *Astron. Astrophys.*, *299*, 885.

Jackson, B. V., and P. L. Hick (1994), Three-dimensional reconstruction of coronal mass ejections, in *Third SOHO Workshop on Solar Dynamic Phenomena and Solar Wind Consequences*, ESA SP-373, p. 199, Eur. Space Agency, Paris.

Jackson, B. V., and P. Hick (2000), Three dimensional tomography of heliospheric features using global Thomson scattering data, *Adv. Space Res.*, *25*(9), 1875.

Jackson, B. V., and P. P. Hick (2002), Corotational tomography of heliospheric features using global Thomson scattering data, *Solar Phys.*, *211*, 344.

Jackson, B. V., and P. P. Hick (2004), Three-dimensional tomography of interplanetary disturbances, in *Solar and Space Weather Radiophysics Current Status and Future Developments*, *ASSL 314*, edited by D. G. Gary and C. U. Keller, p. 355, Springer, New York.

Jackson, B. V., R. A. Howard, N. R. Sheeley Jr., D. J. Michels, M. J. Koomen, and R. M. E. Illing (1985), Helios spacecraft and Earth perspective observations of three looplike solar mass ejections, *J. Geophys. Res.*, *90*, 5075.

Jackson, B. V., P. L. Hick, M. Kojima, and A. Yokobe (1997), Heliospheric tomography using interplanetary scintillation observations, *Adv. Space Res.*, *20*(1), 23.

Jackson, B. V., P. L. Hick, M. Kojima, and A. Yokobe (1998), Heliospheric tomography using interplanetary scintillation observations: 1. Combined Nagoya and Cambridge observations, *J. Geophys. Res.*, *103*, 12,049.

Jackson, B. V., A. Buffington, and P. P. Hick (2001), A heliospheric imager for solar orbiter, in *Proceedings of Solar Encounter: The First Solar Orbiter Workshop, Puerto de la Cruz, Tenerife, Spain, 14–18 May 2001*, ESA SP-493, p. 251, Eur. Space Agency, Paris.

Jackson, B. V., P. P. Hick, and A. Buffington (2002), Time-dependent tomography of heliospheric features using the three-dimensional reconstruction techniques developed for the Solar Mass Ejection Imager (SMEI), *Proc. SPIE*, *4853*, 23.

Jackson, B. V., et al. (2004), The Solar Mass Ejection Imager (SMEI) mission, *Solar Phys.*, *225*, 177.

Kojima, M., and T. Kakinuma (1987), Solar-cycle evolution of solar-wind speed structure between 1973 and 1985 observed with the interplanetary scintillation method, *J. Geophys. Res.*, *92*, 7269.

Kojima, M., K. Asai, P. L. Hick, B. V. Jackson, M. Tokumaru, H. Watanabe, and A. Yokobe (1997), Solar wind structure at 0.1–1 AU reconstructed from IPS observations using tomography, in *Robotic Exploration Close to the Sun: Scientific Basis*, edited by S. R. Habbal, *AIP Conf. Proc.*, *385*, 97.

Kojima, M., M. Tokumaru, H. Watanabe, A. Yokobe, K. Asai, B. V. Jackson, and P. L. Hick (1998), Heliospheric tomography using interplanetary scintillation observations: 2. Latitude and heliocentric distance dependence of solar wind structure at 0.1–1 AU, *J. Geophys. Res.*, *103*, 1981.

MacQueen, R. M. (1993), The three-dimensional structure of "loop-like" coronal mass ejections, *Solar Phys.*, *145*, 169.

Mizuno, D. R., et al. (2005), Very high-altitude aurora observations with the Solar Mass Ejection Imager, *J. Geophys. Res.*, *110*, A07230, doi:10.1029/2004JA010689.

Munro, R. H. (1977), Coronal transients: Arches or bubbles?, paper presented at Topical Conference on Solar and Interplanetary Physics, Univ. of Ariz., Tucson, Ariz.

Skoug, R. M., J. T. Josling, J. T. Steinberg, D. J. McComas, C. W. Smith, N. F. Ness, Q. Hu, and L. F. Burlaga (2004), Extremely high speed solar wind: 29–30 October 2003, *J. Geophys. Res.*, *109*, A09102, doi:10.1029/2004JA010494.

Tappin, S. J., et al. (2004), Tracking a major interplanetary disturbance with SMEI, *Geophys. Res. Lett.*, *31*, L02802, doi:10.1029/2003GL018766.

Tokumaru, M., M. Kojima, K. Fujiki, M. Yamashita, and D. Baba (2005), Interplanetary consequences caused by the extremely intense solar activity during October–November 2003, *J. Geophys. Res.*, *110*, A01109, doi:10.1029/2004JA010656.

Wang, X., P. P. Hick, B. V. Jackson, and M. Bailey (2003), Visualization of remotely-sensed heliospheric plasmas for space weather applications, *Proc. SPIE*, *5171*, 280.

Wilson, D. C. (1977), The three-dimensional solar corona—A coronal streamer, Ph.D. thesis, Univ. of Colo., Boulder, Colo.

Zidowitz, S., B. Inhester, and A. Epple (1995), The three-dimensional structure of the solar corona, in *Solar Wind Eight*, edited by D. Winterhalter et al., *AIP Conf. Proc.*, *382*, 165–168.

_____

A. Buffington, P. P. Hick, B. V. Jackson, and X. Wang, Center for Astrophysics and Space Sciences, University of California, San Diego, 9000 Gilman Drive, La Jolla, CA 92093-0111, USA. (bjackson@cass01.ucsd.edu)

D. Webb, Institute for Space Research, Boston College, Chestnut Hill, MA, USA.